PS/LP Note 2000-01 (MD)
CTF3 Tech. Note 2000-09 (MD-LPI)
22 May 2000

LIL bunch length and lattice parameters measurements in March 2000

R. Corsini, A. Ferrari, L. Rinolfi, T. Risselada, P. Royer, F. Tecker

CERN, Switzerland

Abstract

Several studies with the LIL machine have been done during the March 2000 MD session. Bunch length and lattice functions measurements were performed. Preliminary measurements of the bunch length gave a value of 7 ps at low charge, and an uncorrelated energy spread was observed in the data. A normalized rms beam emittance of about 40 π mm.mrad was measured in both the horizontal and vertical directions, and a fair agreement between the experimental data and the predicted values of the lattice functions was obtained.

1 Introduction

Within the framework of the CLIC Test Facility (CTF3) project [1], several studies with the current LEP Pre-Injector (LPI) have been performed [2, 3]. In March 2000, a complete week was dedicated to beam studies in LIL. The two main topics were the bunch length measurements, as well as the beam emittance and Twiss parameters measurements, at various energies.

The precise knowledge of the bunch length is a critical issue for the combination scheme in CTF3. In order to achieve an efficient frequency multiplication, this bunch length has to be kept small and constant. Up to now, the longitudinal distribution in LIL or EPA is measured using a streak camera. In LIL, the OTR (Optical Transition Radiation) is recorded by the streak camera, while the synchrotron light is used in EPA. Here, a different method, based on the analysis of the energy spectrum, was used in order to measure the bunch length at 200 MeV in LIL.

One of the first steps in the construction of the CLIC Test Facility CTF3 is the transformation of LPI into an isochronous ring fed by the LIL accelerator. For this latter one, several changes are required and a good knowledge of its lattice functions is thus necessary. In particular, one may wonder if the computer codes used to design the new linac are reliable enough. In March 2000, we performed some measurements with wire beam scanners (WBS) in three different points of LIL, in order to derive the emittance of the beam ϵ, as well as the Twiss parameters β and α, in both the horizontal and the vertical directions. For this kind of measurements, we show that the computation of the beam energy, as well as a good setting of the wire beam scanners, are of first importance.

In addition to the bunch length and lattice functions measurements in LIL, the EPA closed orbit was checked, in order to make sure that it is acceptable for the operation of LEP in year 2000.

In the following of this paper, Section 2 gives more details on the method used to measure the bunch length in LIL. Section 3 deals with the derivation of the Twiss parameters and the beam emittance in three points of LIL. In Section 4, we summarize the tests performed on the wire beam scanners and the rf peak power meters. Section 5 briefly describes the measurement of the EPA closed orbit. Finally, in Section 6, we give a brief summary on the March 2000 MD session, as well as a list of the future measurements to be done.

2 Bunch length measurements

2.1 Measurements principle

The technique described in the following is based on the relationship between the energy spread and the phase of the accelerating rf wave. Provided the charge is low enough, beamloading between the buncher and the measurement point is negligible, and the main contribution to the energy spread for a given bunch length depends on the position of the

bunch on the rf cosine wave. From the experimental point of view, the phase between the buncher and the accelerating structures is varied, while the energy spectra are monitored downstream in a spectrometer. The properties of the longitudinal distribution are then extracted from the energy spectra. Assuming a gaussian shape for the bunches and an uncorrelated energy spread, the experimental values are compared to calculations and the bunch length is eventually estimated.

2.2 Theoretical background

The longitudinal bunch distribution is assumed to be a gaussian function of mean μ and standard deviation σ :

$$n(t) = \frac{1}{\sigma\sqrt{2\pi}} e^{-\frac{(t-\mu)^2}{2\sigma^2}} \tag{1}$$

where μ is the variable corresponding to the phase (in seconds) of the rf wave. For instance, $\mu = 0$ would give a bunch centered on the crest of the cosine wave. The energy at the measurement point is given by the rf function :

$$E(t) = E_0 \cos(2\pi\nu t) = E_0 \cos(\omega t) \tag{2}$$

where E_0 is the maximum energy. Inverting equation (2) gives :

$$t(E) = \frac{1}{\omega} \arccos\left(\frac{E}{E_0}\right). \tag{3}$$

Inserting (3) into (1) and using the derivation of (3), the transformation :

$$n(t)dt \longrightarrow n(t(E)).\frac{dt(E)}{dE}dE = n(E)dE \tag{4}$$

leads to the energy distribution $n(E)$ as a function of μ and σ. Let us now define the normalization factor N, which is a function of the phase, by :

$$\begin{aligned} N(\mu) &= \int_{-E_0}^{E_0} n(t(E)).\frac{dt(E)}{dE}dE \\ &= \int_{-E_0}^{E_0} \frac{dE}{E_0\omega\sigma\sqrt{2\pi}} \frac{1}{\sqrt{1-(\frac{E}{E_0})^2}} e^{-\frac{(t(E)-\mu)^2}{2\sigma^2}}. \end{aligned} \tag{5}$$

Then, the final normalized distribution $D(E)$ is given by the ratio :

$$D(E) = \frac{n(E)}{N}. \tag{6}$$

From this analytical distribution, the rms energy spread and the mean energy are calculated through the usual definitions :

$$\begin{aligned} E_{mean} &= \int_{-E_0}^{E_0} E\, D(E)\, dE \\ \sigma_E^2 &= \int_{-E_0}^{E_0} (E - E_{mean})^2\, D(E)\, dE. \end{aligned}$$

Figure 1 shows the energy distribution for two bunches : the first one is on the crest (no phase shift) and the other one has a phase shift of $\frac{2\pi}{5}$. The rms bunch length is set to $\sigma = 8.5$ ps, the maximum energy is $E_0 = 200$ MeV and the rf frequency is 2.998 GHz. Particles experiencing a negative energy are decelerated by the rf wave.

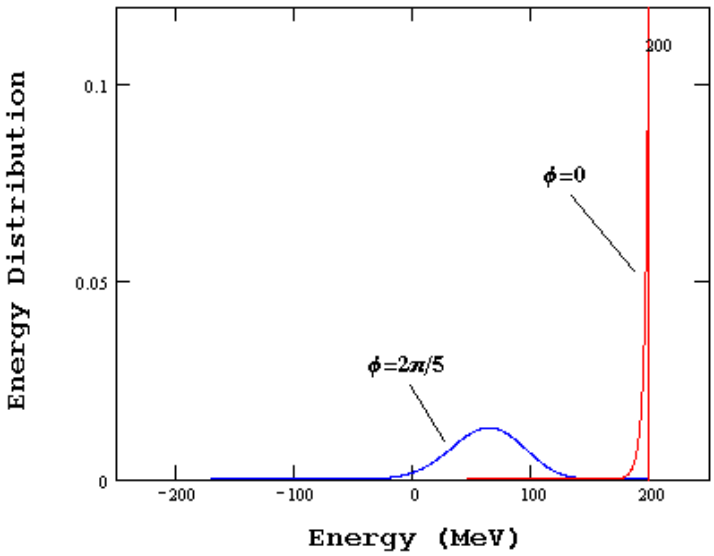

Figure 1: Energy distribution for bunches with $\Phi = 0$ and $\Phi = \frac{2\pi}{5}$.

As reported and calculated in [4], the phase of the particles is assumed to remain constant from the output of the buncher to the measurement point, which is not fully true at low energy. Therefore, the agreement between calculated and measured spectra is expected to be better at high energy.

2.3 Experimental studies

2.3.1 Beamloading

The contribution of the beamloading to the energy spread must be negligible to ensure the efficiency of the method. By increasing the bias voltage applied to the extraction grid of the gun (using the knob VL.GUN-BIAS), the charge in the pulse is reduced. At low charge, the contribution of the beamloading to the mean energy and to the energy spread is minimum. To check this effect, we varied the pulse charge using VL.GUN-BIAS, while keeping the pulse length (controlled by the knob VL.GUN-PULSE) constant, and we measured the mean energy and the energy spread in SEM15.

Our results are shown on figures 2 and 3, where they are compared with previous measurements and with theoretical expectations using the nominal beamloading parameter $K_{BL} = 0.196$ MeV/c per structure [5].

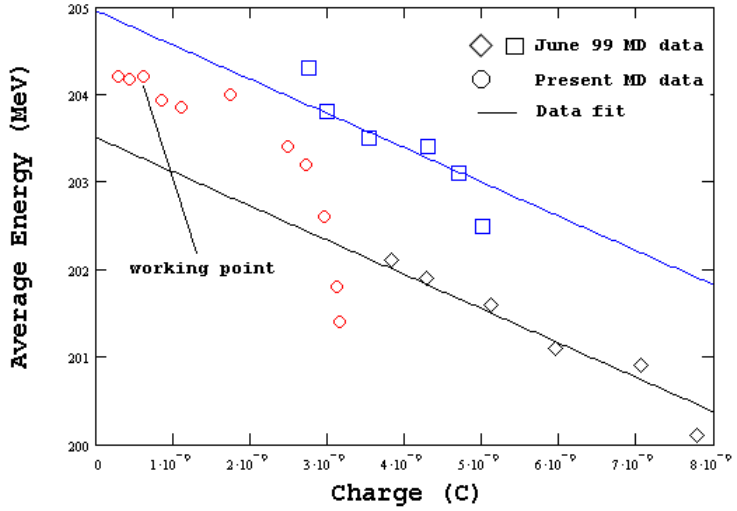

Figure 2: Mean energy as a function of the pulse charge.

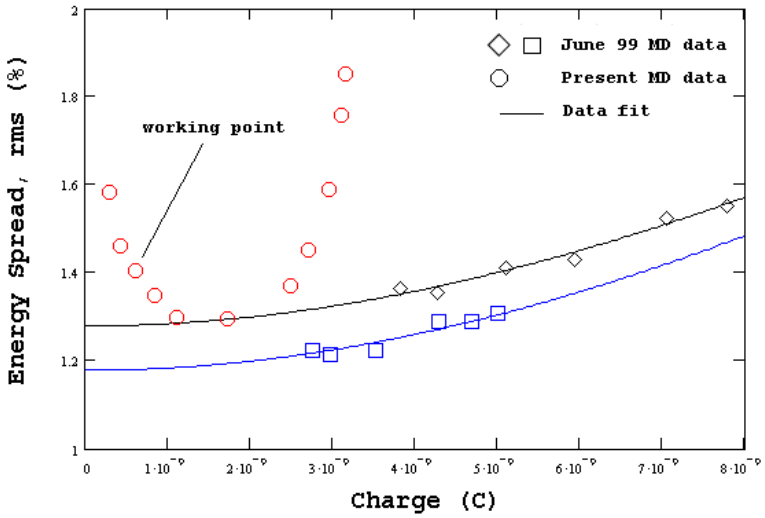

Figure 3: Energy spread as a function of the pulse charge.

The previous measurements were performed with a different method to vary the total charge, namely changing VL.GUN-PULSE and keeping VL.GUN-BIAS constant. In this way, the bunch charge is constant and the bunching system always works in the same conditions (optimized for a smaller energy spread in principle). On the other hand, by changing VL.GUN-BIAS, we change the charge per bunch, and possibly the beam energy at the exit of the gun. Therefore, for large variations, the bunching system does not work in a proper way anymore. This explains the discrepancy between the measurements. For instance, the large variation of the energy spread in our data is due to the mismatch with the bunching system and not to beamloading. It can also be noticed that the bunching system was probably not optimized for our working point (0.5 nC/pulse), but rather for

a higher charge (about 1.5 nC/pulse). This is not important for the measurement itself, although it could mean that a shorter bunch length could be obtained. By looking at the theoretical predictions on figure 3 (see the flat curve below 3 nC/pulse), one can conclude that the beamloading contribution to the energy spread is small at our working point.

2.3.2 Data acquisition

The phase between the buncher and the accelerating structures is tuned using the knob VL.B-PHAS, which changes the relative phase of the buncher with respect to the accelerating cavities. The energy spectra are monitored in SEM15 at an energy around 200 MeV, using the bending magnet BSP15.

First Method :

The tuning range of the phase is limited by the horizontal acceptance in the spectrometer : the further from the crest, the larger the energy spread and the wider the spectrum in the spectrometer. Within this limitation, four points on each side of the crest are recorded. For each point, the current value in BSP15 is adjusted to have a centered distribution in the spectrometer before taking the data. Figure 4 shows the mean energy as a function of the phase shift introduced by the knob VL.B-PHAS. As expected, the points describe the top of a cosine wave :

$$E(\Phi) = A + B\cos(\Phi) \tag{7}$$

where $\Phi = 0$ when the bunch is on the crest, corresponding to the maximum acceleration and the minimum energy spread. The cosine fit gives the phases of the points, which are respectively 9.7, 14.6, 19.5, 24.3 degrees on each side of the crest.

For each point, the spectrum is stored and a systematic correction matrix is applied to cope with an internal error of the normalization process in the SEM-grid program. Since the spectra are available, the mean energy and rms energy spread are directly computed from the values read for each wire of the SEM-grid.

Let w_i be the weight for the measurement i and x_i the position of the wire i in the SEM-grid. Then, for n measurement points, the statistical data are :

$$\begin{aligned} \overline{X} &= \frac{1}{N}\sum_{i=1}^{n} w_i x_i \\ \sigma^2 &= \frac{1}{N}\sum_{i=1}^{n} w_i (x_i - \overline{X})^2 \end{aligned} \tag{8}$$

where N is the normalization factor given by :

$$N = \sum_{i=1}^{n} w_i. \tag{9}$$

The results of these calculations are given in table 1.

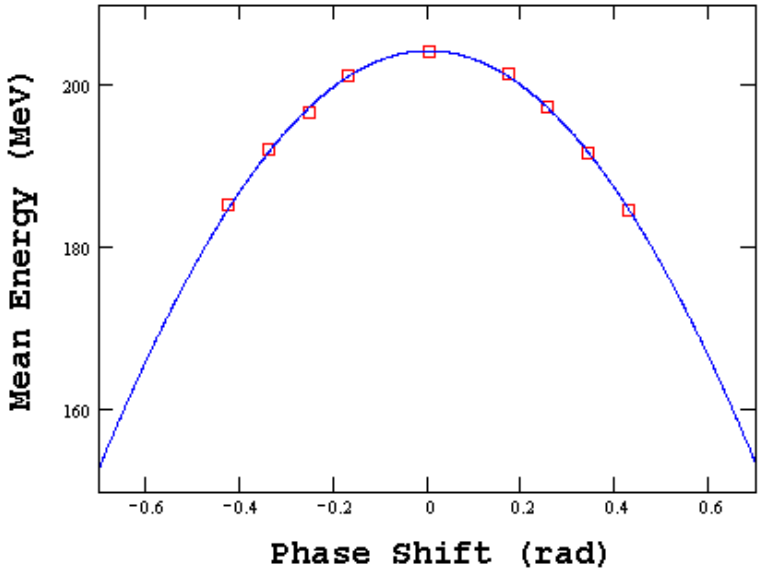

Figure 4: Mean Energy as a function of the phase shift on the rf wave.

Φ (°)	E^{exp}_{mean} (MeV)	σ^{exp}_{E} (MeV)
-24.3	183.4	5.0
-19.5	191.5	4.5
-14.6	196.9	3.8
-9.7	201.4	3.1
0	204.8	2.1
+9.7	201.4	3.2
+14.6	197.6	3.7
+19.5	191.4	4.7
+24.3	183.8	5.4

Table 1: Experimental values of the mean energy and the energy spread for various phase shifts.

Second Method :

If the horizontal acceptance of the spectrometer is not large enough to cover the whole spectrum at high phase shifts, the tails of the spectrum are cut, and the rms value is reduced. To cope with this, two new sets of measurements are taken for $\Phi = 0°$ and $\Phi = -19.5°$, by varying step by step the current value of BSP15, in order to scan the whole spectrum with the central wire of SEM15. The final spectrum is then rebuilt by juxtaposing each step of the measurement. Figure 5 show the final spectra as a function of the current in BSP15 for both phases, as well as a gaussian fit, giving the rms bunch length in terms of the current in BSP15.

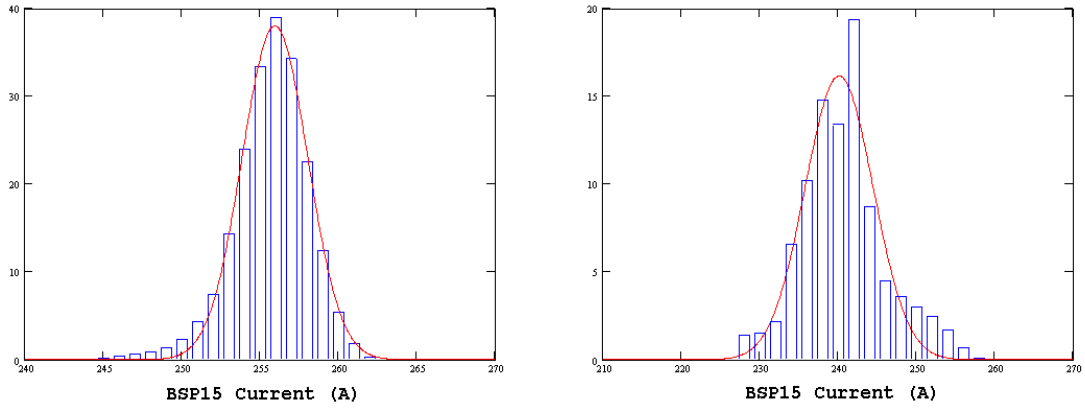

Figure 5: Energy spectrum at $\Phi = 0°$ (left-hand side plot) and at $\Phi = 19.5°$ (right-hand side plot), as a function of the current in BSP15.

A linear relationship

$$E(I) = \kappa I \tag{10}$$

between the current I in BSP15 (in Amps) and the mean energy E (in MeV) is extracted from a linear fit which gives $\kappa = 0.801$ (corresponding to figure 6).

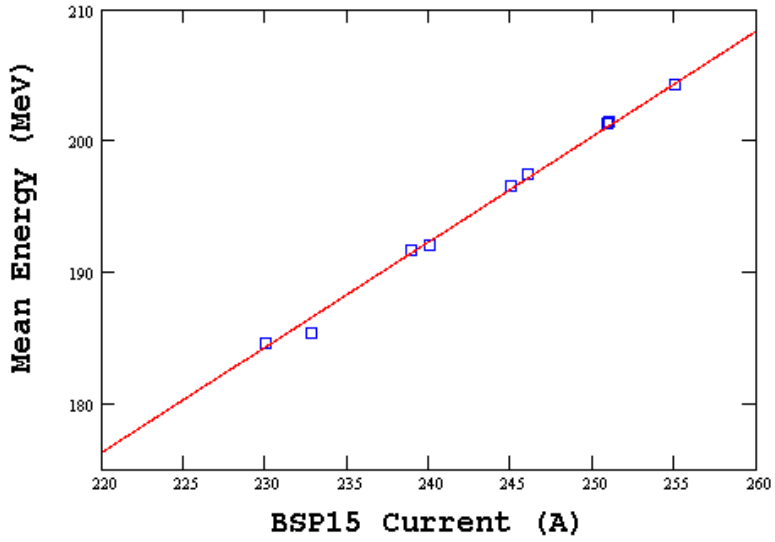

Figure 6: Linear relationship between energy and current in BSP15.

For each phase, the current in BSP15 is varied so that the mean energy coincides with the energy measured by the central wire of the grid. The relationship is consistent with the values used by the on-line computation program. The mean energy and rms energy spread read from the fit function in terms of the current in BSP15 can now be expressed in terms of the energy and are shown in table 2.

Φ (°)	E_{mean}^{fit} (MeV)	σ_E^{fit} (MeV)
0	205.0	1.7
-19.5	192.3	3.5

Table 2: Experimental values for the mean energy and the energy spread with complete beam profiles and fit function.

In addition, the mean value and the standard deviation are calculated using equations (8). The results are given in table 3. These values obtained with the statistical calculations are retained in the following for coherence with the first method where the same calculations were performed.

Φ (°)	E_{mean}^{stat} (MeV)	σ_E^{stat} (MeV)
0	204.8	1.9
-19.5	192.8	4.3

Table 3: Experimental values for the mean energy and the energy spread with complete beam profiles and statistical calculations.

2.4 Results

Simple Model :

The simplest model is to assume that all the energy spread is caused by the phase shift without any other contribution. Knowing the phase shift, a comparison between the energy spread read from the spectrometer and the calculated spread, as seen in section 2.2, is possible. Table 4 compares the experimental (from table 1) and calculated energy spreads corresponding to the various phase shifts with a rms bunch length $\sigma_L = 1.95$ mm, or 15 ps FWHH. This value of the bunch length, as well as the value of $E_0 = 206$ MeV in equation (2), are chosen to match the experimental data to the calculations on the crest point ($\Phi = 0$).

Φ (°)	E_{mean}^{exp} (MeV)	σ_E^{exp} (MeV)	E_{mean}^{cal} (MeV)	σ_E^{cal} (MeV)
0	204.8	2.1	204.5	2.1
$\pm$ 9.7	201.4/201.4	3.2/3.1	201.2	4.8
$\pm$ 14.6	197.6/196.9	3.7/3.8	197.7	6.6
$\pm$ 19.5	191.4/191.5	4.7/4.5	192.9	8.6
$\pm$ 24.3	183.8/183.4	5.4/5.0	186.3	10.5

Table 4: Calculated and experimental values of the mean energy and the energy spread for various phase shifts.

Although the values of the mean energy are relatively well confirmed by the calculations, the behaviour of the energy spread differs drastically and this simple model does not seem to fit the data.

Model with an uncorrelated energy spread :

The longitudinal spectra in the spectrometer are recorded in a dispersive region and are derived from the transverse beam size. However, the dispersion is not the only contribution to the beam size. Although the emittance is small, the contribution of the β-function in the spectrometer might not be negligible. The uncorrelated energy spread at the output of the buncher should also be taken into account (as noticed in section 2.3.1). Eventually, the beam jitter contributes to the beam size read by the spectrometer. Since the mean energies and the rms energy spreads are symmetric with respect to the crest, no effect of the phase motion between the buncher and the measurement point is expected.

All these contributions are gathered in a systematic, global uncorrelated energy spread σ_0. The experimental values σ_E are then corrected as follows :

$$\sigma_{corr}^2 = \sigma_E^2 + \sigma_0^2. \tag{11}$$

The results are presented on figure 7 and in table 5.

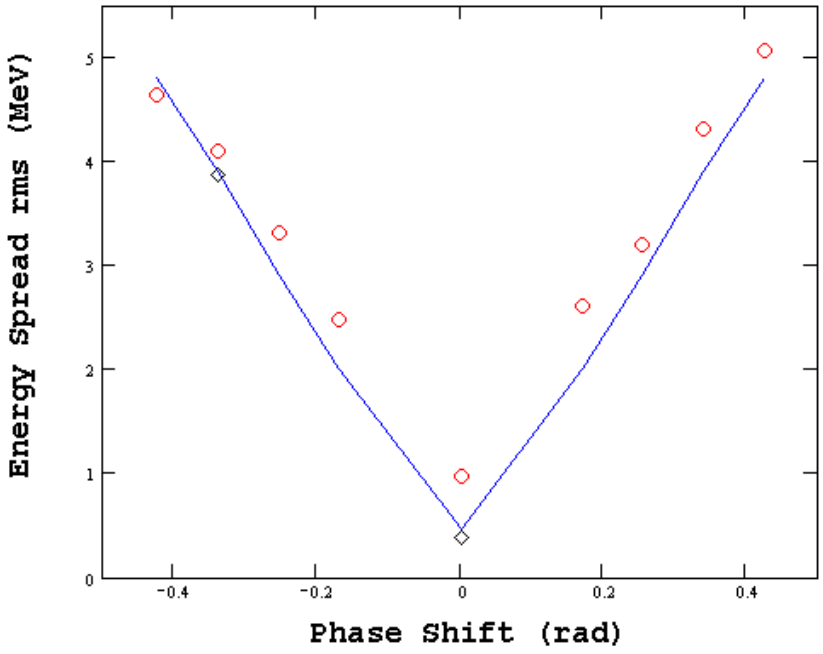

Figure 7: Corrected and calculated energy spreads with bunch length 7 ps FWHH.

Φ (°)	σ_E^{exp} (MeV)	σ_E^{corr} (MeV)	σ_E^{cal} (MeV)
0	2.1	0.97	0.46
± 9.7	3.1/3.2	2.6/2.5	2.0
± 14.6	3.7/3.8	3.2/3.3	2.9
± 19.5	4.7/4.5	4.3/4.1	3.9
± 24.3	5.4/5.0	5.1/4.6	4.8

Table 5: Raw data for energy spreads, corrected experimental values (σ_0 = 1.86 MeV) and calculated values (σ_L = 3.00 ps, 7 ps FWHH)

First, the correction is performed on the first set of data (round points) and on the two scanned profiles (diamond-shaped points), corresponding to tables 1 and 3. Then, the energy spreads are calculated as explained in section 2.2 and the points are linked (see the two lines). In order to have the correct fit on the points, the bunch length FWHH is 7 ps and the uncorrelated energy spread is 1.86 MeV. The alignment of all the points on each side of the crest point shows a good agreement between both techniques of data acquisition. The alignment of the lines on the points shows that the data from the spectrometer are consistent with a very short bunch length (7 ps FWHH) and an uncorrelated energy spread resulting from various effects. The slope of the line is very sensitive to the bunch length, which gives to this method a precision of the order of one pico-second. The discrepancy between the calculated values and the experimental points is larger for the points close to the crest because the spectra are narrower and the number of useful wires in the SEM-grid is smaller, so that the precision is lower. Close to $\Phi = 0$, the values given when scanning the whole spectrum with one wire (second method of data acquisition) are more accurate.

Here, the bunch length of 7 ps FWHH corresponds to a bunch with low charge. In case of a higher charge, some previous data show a larger bunch length [6]. The LIL microbunch structure measured using a streak camera is shown on figure 8 with a bunch length of 14 ps, for a charge of 0.4 nC per bunch.

2.5 Conclusion

Assuming a very simple model that includes an uncorrelated energy spread, a good agreement is found between measurements and calculations. At low charge, the bunch length is around 7 ps FWHH and the amount of uncorrelated energy spread is 1.86 MeV. Moreover, the precision of the method is close to the pico-second. In the future, a new set of measurements at 500 MeV would help validate this method and calibrate the various parameters found here. The cross-check with the value of the bunch length measured with the streak camera in the linac is also mandatory, although the accuracy of the streak camera is probably lower than what is needed here.

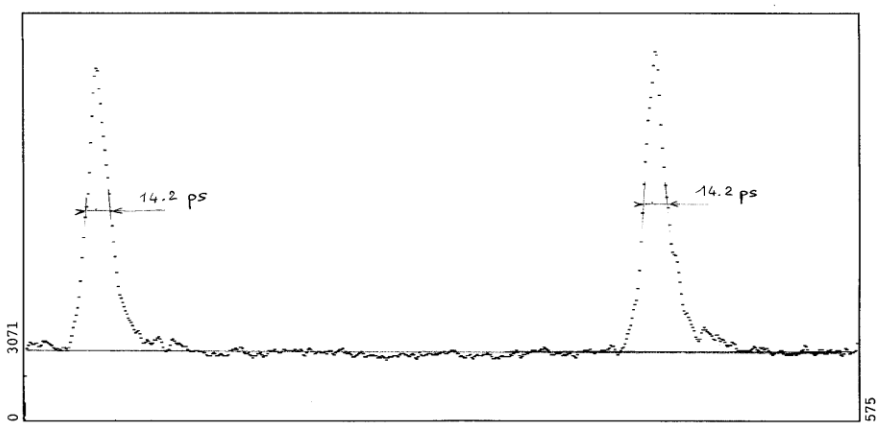

Figure 8: LIL microbunch structure as measured using a streak camera.

3 Lattice functions measurements

3.1 Description of the tested section of LIL

The LIL machine is divided into two long sections called LIL-V and LIL-W. The first one extends from the source to the electron-positron conversion target, while the second one extends from the target to the beginning of the EPA transfer line.

In the following, we will be mainly interested in the end of the LIL-V section and the whole LIL-W section, with two regions of interest : the first one is between the quadrupoles QLB151 and QNM273, while the second one is between QNM273 and QNM363 (see figure 9). The beam emittance and the Twiss parameters are measured at the entrance of the three latter quadrupoles.

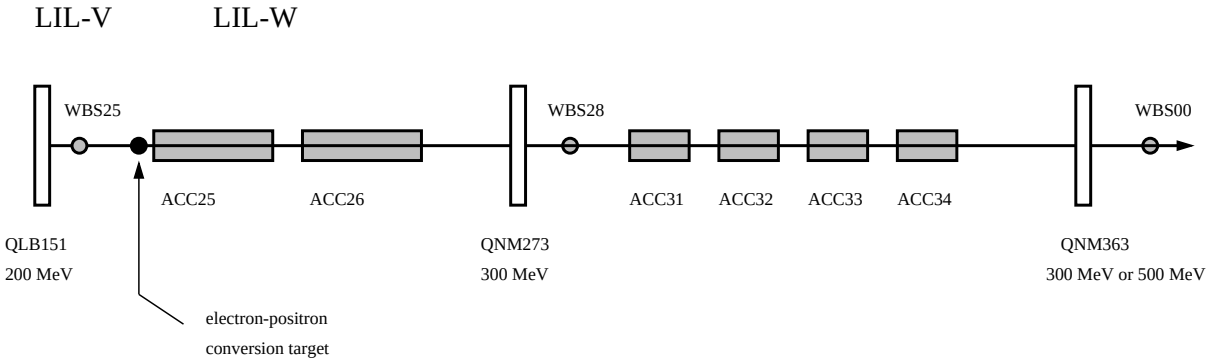

Figure 9: Schematic layout of the LIL section which has been tested in March 2000. Only the most relevant elements are shown here (see text for more details).

Some other quadrupoles, as well as two long solenoids are installed along LIL. Their main characteristics are shown in tables 6 and 7. In these tables, the currents which are displayed correspond to the conditions for LEP operation, but some of them were modified or varied in order to perform some measurements.

Between QLB151 and QNM363, there are 12 accelerating sections with a length of 4.572 m each (ACC25 to ACC36). But only 6 of them receive some rf-power in order to increase the beam energy from 205.9 MeV at the end of LIL-V up to 502.6 MeV at the end of LIL-W : the total measured energy gain in ACC25 and ACC26 is 104.6 MeV, while it is 192.1 MeV in ACC31, ACC32, ACC33 and ACC34. The layout and the main characteristics of these 6 accelerating sections are as follows :

- the center of ACC25 (respectively ACC26) is at 5.90 m (respectively 10.80 m) from the entrance of QLB151. The magnetic fields of both SNL25 and SNL26 are thus superposed to the constant electric field of ACC25 and ACC26.
- the centers of ACC31, ACC32, ACC33 and ACC34 are respectively at 21.736 m, 26.886 m, 31.936 m and 37.086 m from the entrance of QNM273. These accelerating sections work with LIPS, so the electric field is not constant along the beam path. Moreover, the magnetic fields of some quadrupoles are superposed to it.

While there is always rf-power in ACC25 and ACC26, we performed a few measurements without any energy gain in LIL-W.

Name	Length (mm)	Polarized current (A)	Calibration (Gauss/A)	Aperture (mm)	Distance in m to entrance of QLB151
QLB1	220	+ 54.60	16.24	29.0	0.110
QLB2	220	- 53.00	16.24	29.0	0.390
QLB3	220	- 53.00	16.24	29.0	0.670
QLB4	220	+ 54.60	16.24	29.0	0.950
SNL25	5025	670.02	5.042	-	5.878
SNL26	4860	670.02	5.042	-	10.820
A271	220	+ 6.00	72.50	29.0	13.420
A272	220	- 9.88	72.50	29.0	13.720
M271	328	+ 96.11	12.56	78.5	14.860
M272	328	- 111.50	12.56	78.5	15.340
M273	328	+ 109.14	12.56	78.5	16.363

Table 6: Main characteristics of the quadrupoles and the solenoids along LIL between QLB151 and QNM273.

Name	Length (mm)	Polarized current (A)	Calibration (Gauss/A)	Aperture (mm)	Distance in m to entrance of QNM273
M273	328	+ 109.14	12.56	78.5	0.164
F271	328	- 160.07	12.56	78.5	0.644
F272	328	+ 160.07	12.56	78.5	1.350
F273	328	- 160.07	12.56	78.5	1.975
F274	328	+ 160.07	12.56	78.5	2.572
QLB28	220	- 55.00	16.24	29.0	3.371
F281	328	+ 160.07	12.56	78.5	4.107
F282	328	- 160.07	12.56	78.5	4.921
F283	328	+ 160.07	12.56	78.5	5.791
F284	328	- 160.07	12.56	78.5	6.721
F285	328	+ 160.07	12.56	78.5	7.714
QLB29	220	- 55.00	16.24	29.0	8.786
F291	328	+ 128.99	12.56	78.5	9.881
F292	328	- 128.99	12.56	78.5	11.052
F293	328	+ 128.99	12.56	78.5	12.286
F294	328	- 128.99	12.56	78.5	13.522
F301	328	+ 128.99	12.56	78.5	14.966
F302	328	- 128.99	12.56	78.5	16.466
F303	328	+ 128.99	12.56	78.5	18.072
Q31a	328	- 128.99	12.56	78.5	19.797
Q31b	328	+ 128.99	12.56	78.5	21.524
Q31c	328	- 128.99	12.56	78.5	23.254
Q32a	328	+ 128.99	12.56	78.5	24.984
Q32b	328	- 129.08	12.56	78.5	26.714
Q32c	328	+ 129.08	12.56	78.5	28.444
Q33a	328	- 129.08	12.56	78.5	30.174
Q33b	328	+ 129.08	12.56	78.5	31.904
Q33c	328	- 129.08	12.56	78.5	33.644
Q34a	328	+ 129.08	12.56	78.5	35.404
Q34b	328	- 129.08	12.56	78.5	37.204
Q34c	328	+ 129.08	12.56	78.5	39.032
F351	328	- 129.08	12.56	78.5	41.084
F352	328	+ 129.08	12.56	78.5	43.244
F361	328	- 129.08	12.56	78.5	45.464
F362	328	+ 129.08	12.56	78.5	47.724
M363	328	- 84.01	12.56	78.5	48.854

Table 7: Main characteristics of the quadrupoles along LIL between QNM273 and QNM363.

3.2 Experimental method to measure ϵ, β and α

In this section, we describe in detail the method used to compute the beam emittance and the Twiss parameters. For this purpose, we first remind the reader of a few useful equations. In transverse beam dynamics, the σ matrix describes the behaviour of a group of particles and, in both the horizontal and the vertical directions, it is defined as :

$$\sigma_{x,y} = \epsilon_{x,y} \cdot \begin{pmatrix} \beta_{x,y} & -\alpha_{x,y} \\ -\alpha_{x,y} & \gamma_{x,y} \end{pmatrix} \text{ where } \gamma = \frac{1+\alpha^2}{\beta}. \tag{12}$$

The square roots of the diagonal terms of this matrix are a measure of the beam size in the x and x' (or y and y') coordinates, while the off-diagonal terms are a measure of the correlations between x and x' (or y and y').

One usually measures ϵ, β and α at the entrance of a given quadrupole Q, which is upstream a wire beam scanner WBS. If R is the transfer matrix between the entrance of Q and WBS, then one has :

$$\sigma(WBS) = R\sigma(Q)R^T. \tag{13}$$

Thus, by measuring the beam profile with WBS in both the x and y directions, and by computing its root mean square (rms), one has access to the square root of $\sigma_{11}(WBS)$. It is a function of ϵ, β and α at the entrance of Q, but also of R and therefore of the normalized gradient of Q, which is defined as :

$$K_{x,y}(Q) = \frac{1}{B\rho} \cdot \left(\frac{\partial B_{y,x}}{\partial x, y} \right). \tag{14}$$

As a result, we proceeded as follows to measure ϵ, β and α :

1. For a given current in Q, and thus for given values of $K_x(Q)$ and $K_y(Q)$, one calculates the rms of the horizontal and vertical beam profiles. For this purpose, we fit the data with a function of the form :

$$f(d) = cste + G_1(d) + G_2(d), \tag{15}$$

where d is the displacement of the wire through the beam, $G_1(d)$ and $G_2(d)$ being two gaussian distributions. Then, we remove the constant term, so we can easily calculate the rms of $G_1(d) + G_2(d)$.

2. We vary the current in Q in order to draw the rms in a given direction vs the normalized gradient in Q. By fitting this plot with an appropriate function (which depends on the layout of the beam line between Q and WBS), it is then possible to derive ϵ, β and α at the entrance of Q.

As for the beam energy E, it can be measured at two positions. At the end of LIL-V, E is easily computed by sending the beam into the MSH15 spectrometer. But, for what concerns the measure of E at the end of LIL-W, the situation is slightly more complicated. The beam must be sent into the transfer line and observed in the MSH20 spectrometer.

Particles thus see the following sequence of elements : BSH00, MTV00, BHZ10, QFW11, BHZ20 and MSH20. The reading of E in MSH20 is reliable only if the beam can be aligned exactly on the reference trajectory, therefore only for a given value of the ratio between the currents in BSH00 and in the BHZ family (containing BHZ10 and BHZ20). Unfortunately, the correct setting of BSH00 could not be checked using the TV screen MTV00, which has the same horizontal phase as BSH00. As a consequence, the setting of the currents in BSH and BHZ had to be done with care and small errors could not be excluded in the measurements of E at the end of LIL-W, especially when there is no energy gain in ACC31-34.

3.3 Summary of the lattice functions measurements in LIL

Here, we describe with more details the various measurements of the beam emittance and of the Twiss parameters, which were performed in LIL between March 6^{th} and 10^{th} 2000. They will be labelled as follows : *date-energy-WBSnumber*. Thus, the measurement performed on March 6^{th} in the wire beam scanner WBS25, with a beam energy of about 200 MeV, is referred to as 0603-200-25. More details on all these measurements can be found in table 8.

Label of the measurement	Date	Mean energy of the beam	Wire Beam Scanner	Quadrupole for the scan	Other remarks
0603-200-25	06/03	205.9 MeV	WBS25	QLB1514	53 A in QLB1523
0703-200-25	07/03	205.9 MeV	WBS25	QLB1514	39 A in QLB1523
0703-300-28a	07/03	310.5 MeV	WBS28	QNM273	53 A in QLB1523, 54.6 A in QLB1514, SNL2526 on
0703-300-28b	07/03	310.5 MeV	WBS28	QNM273	39 A in QLB1514, 39 A in QLB1523, SNL2526 off
0703-300-00	07/03	310.5 MeV	WBS00	QNM363	39 A in QLB1514, 39 A in QLB1523, 109.1 A in QNM273
0803-500-00	08/03	502.6 MeV	WBS00	QNM363	39 A in QLB1514, 39 A in QLB1523, 109.1 A in QNM273
1003-500-00	10/03	502.6 MeV	WBS00	QNM363	39 A in QLB1514, 39 A in QLB1523, 109.1 A in QNM273

Table 8: Summary of the measurements of the beam emittance and the Twiss parameters in LIL in March 2000.

3.4 Analysis of the experimental results and comparison with the simulation

3.4.1 Analysis of 0703-300-28b and 0703-300-00

In this section, we concentrate on the measurements performed in WBS28 and WBS00, when there is no energy gain in LIL-W. This situation is the simplest one to simulate, since only quadrupoles and drifting lines are taken into account.

In a first step, we take the measured energy $E = 310.5$ MeV and we determine the characteristics of the beam at the entrance of QNM273 by analysing 0703-300-28b (here, the emittance corresponds to the geometrical rms of the beam and it is not normalized) :

- $\epsilon_x = 0.068\ \pi$ mm.mrad, $\beta_x = 38.6$ m and $\alpha_x = -10.2$,
- $\epsilon_y = 0.064\ \pi$ mm.mrad, $\beta_y = 83.2$ m and $\alpha_y = +25.0$.

Figure 10 shows the variations of β_x and β_y along the beam trajectory between QNM273 and QNM363. This simulation shows that the amplitudes of the betatron functions reach very low and quite high values.

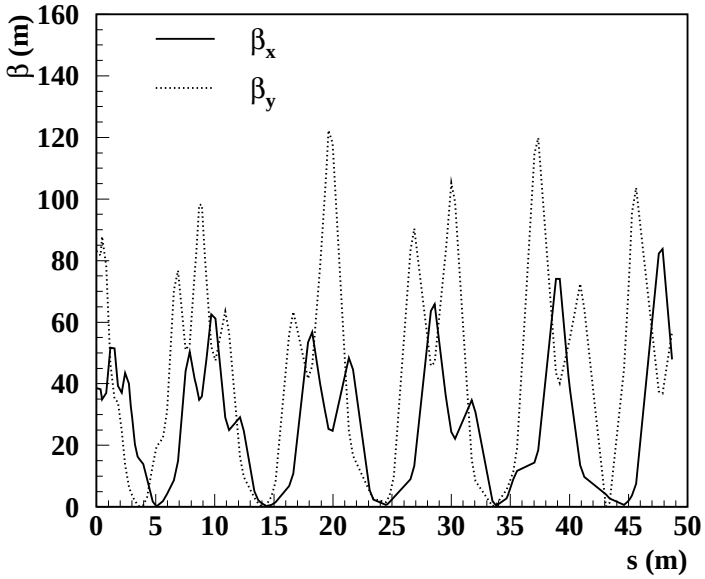

Figure 10: Variations of β_x and β_y along the beam trajectory between QNM273 and QNM363, as simulated with TRANSPORT [7]. Here, the energy of the beam is 310.5 MeV. At the entrance of QNM273, $\beta_x = 38.6$ m and $\alpha_x = -10.2$, $\beta_y = 83.2$ m and $\alpha_x = +25.0$.

On figure 11, one can see that the values predicted for β and α at the entrance of QNM363 strongly depend on E (for a given current, the focusing strengths of the quadrupoles along the beam line are inversely proportional to the beam momentum). The beam has a given

energy spread. Let us assume that the values of β and α measured at the entrance of QNM273 do not depend on E. In a first approximation, one can consider that each energy bin propagates along LIL-W in a slightly different way, so the profiles measured in WBS00 are the superposition of the profiles due to each energy bin.

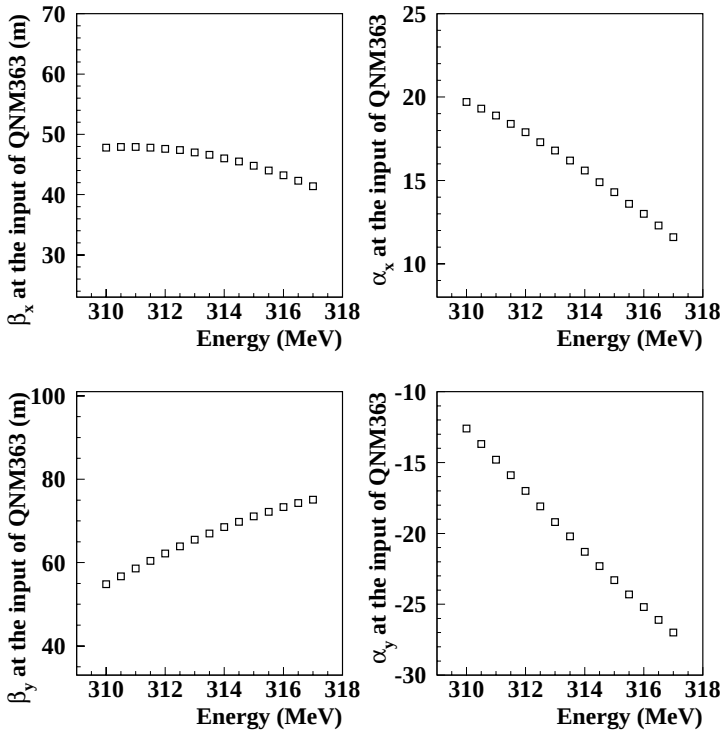

Figure 11: Variations of β_x, α_x, β_y and α_y at the entrance of QNM363 with the beam energy (TRANSPORT simulation). At the entrance of QNM273, one has $\beta_x = 38.6$ m and $\alpha_x = -10.2$, $\beta_y = 83.2$ m and $\alpha_x = +25.0$.

When one wants to take this effect into account, a problem remains : the data taken in WBS00 do not match with the predictions made with the TRANSPORT code, in both the horizontal and the vertical directions, unless the mean energy of the beam is brought to 313.5 MeV. Given the accuracy of the energy measurement at the end of LIL-W, an error of about 1% can not be excluded. Thus, in the following of this paper, we will assume that, at the entrance of QNM273, one has $E_{mean} = 313.5$ MeV and :

- $\epsilon_x = 0.068\ \pi$ mm.mrad, $\beta_x = 39.1$ m and $\alpha_x = -10.1$,
- $\epsilon_y = 0.065\ \pi$ mm.mrad, $\beta_y = 84.2$ m and $\alpha_y = +25.4$.

In these conditions, there is a fair agreement between the TRANSPORT simulations and the data collected in WBS00 when the current in QNM363 is varied, as shown on figure 12 (this measurement is referred to as 0703-300-00).

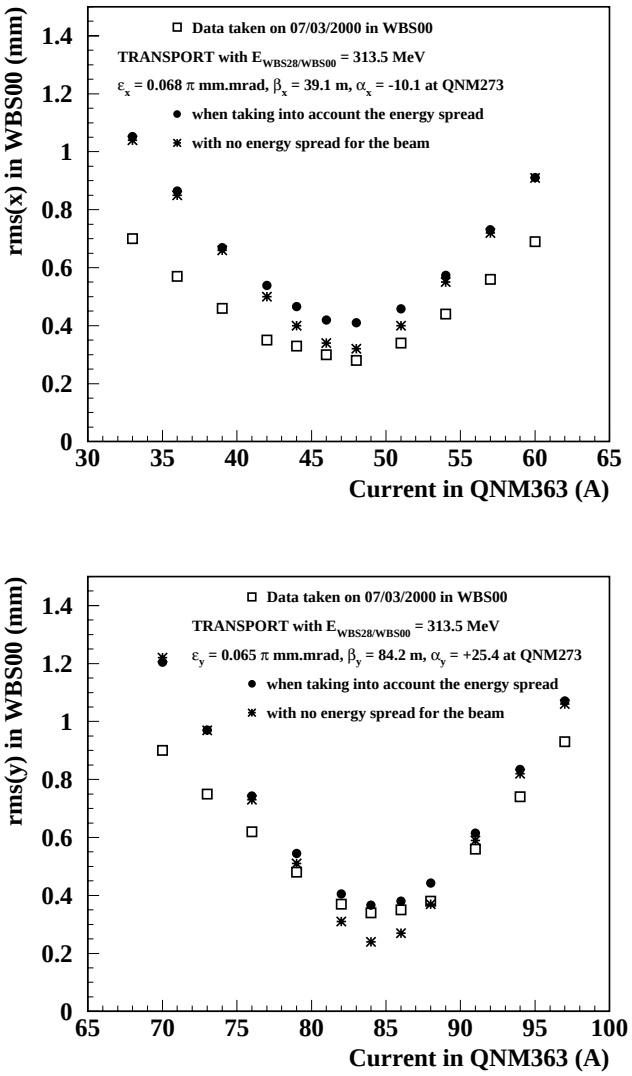

Figure 12: Variations of the rms of the horizontal and vertical beam profiles in WBS00 as a function of the current in QNM363 (TRANSPORT simulations and data). There is no energy gain between QNM273 and QNM363.

3.4.2 Analysis of 0803-500-00 and 1003-500-00

In this section, we look at the same section of LIL as in the previous case, but there is now some rf-power in ACC31, ACC32, ACC33 and ACC34. Two sets of measurements were performed and, as shown in figure 13, they are compatible. As for the simulation of the accelerating sections, one must take into account the elements with a non-uniform electric field. For this purpose, a division into smaller elements, where the electric field remains constant, was done. When a quadrupolar magnetic field and a constant electric field are superposed, we use the following sequence : acceleration up to the center of the quadrupole, drift in the backward direction down to the entrance of the quadrupole,

quadrupole, drift in the backward direction down to the center of the quadrupole, acceleration up to the exit of the quadrupole.

Figure 13 shows that there is a pretty good agreement between the TRANSPORT simulations and the data collected in WBS00, when one varies the current in QNM363.

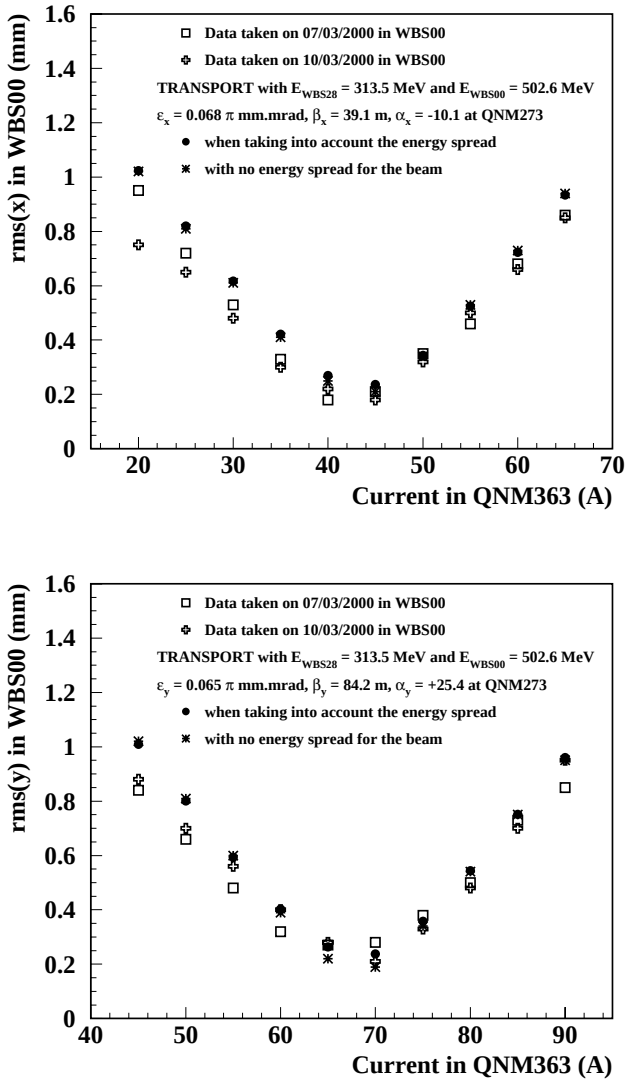

Figure 13: Variations of the rms of the horizontal and vertical beam profiles in WBS00 as a function of the current in QNM363 (TRANSPORT simulations and data). There is an energy gain between QNM273 and QNM363.

As for figure 14, it shows that the dependence of the analysis on the value of the mean energy at QNM273 is weak in the horizontal direction, but still has to be taken into account in the vertical plane.

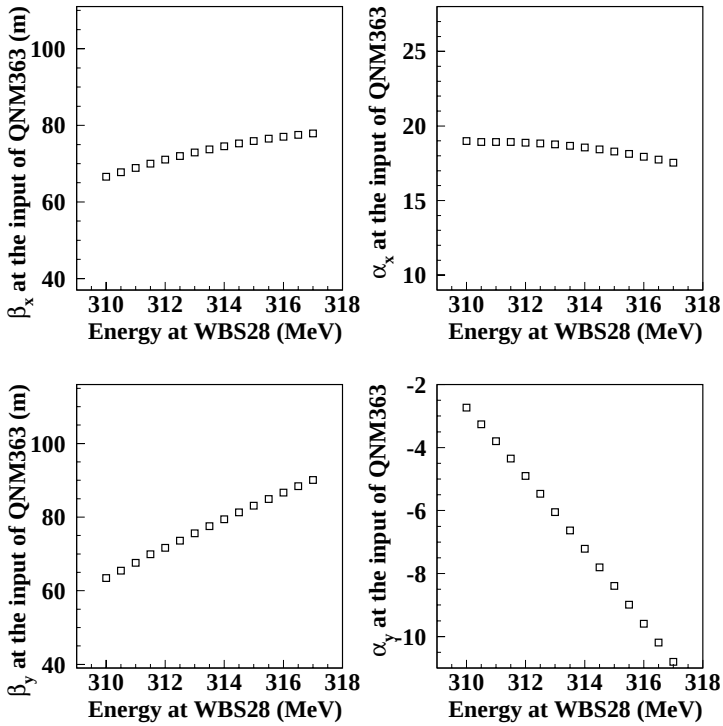

Figure 14: Variations of β_x, α_x, β_y and α_y at the entrance of QNM363 with the beam energy at QNM273 (TRANSPORT simulation). At the entrance of QNM273, one has $\beta_x = 38.1$ m and $\alpha_x = -10.1$, $\beta_y = 84.2$ m and $\alpha_x = +25.4$.

3.4.3 Analysis of 0603-200-25, 0703-200-25 and 0703-300-28a

Two sets of measurements were performed with WBS25, in order to determine the beam emittance and the Twiss parameters at the entrance of QLB151 : in the solenoids SNL25 and SNL26, the magnetic field was either switched off (as for all the other measurements described previously) or switched on. The currents in QLB151, QLB152, QLB153 and QLB154 are different when one goes from one case to the other, so it is necessary to check that the analysis of 0603-200-25 and 0703-200-25 are nevertheless compatible.

When the solenoids are switched on (0603-200-25), the beam emittance and the Twiss parameters computed at the entrance of QLB151 are :

- $\epsilon_x = 0.090$ π mm.mrad, $\beta_x = 23.7$ m and $\alpha_x = -0.45$,
- $\epsilon_y = 0.099$ π mm.mrad, $\beta_y = 28.1$ m and $\alpha_y = -1.56$.

When the solenoids are switched off (0703-200-25), then one finds :

- $\epsilon_x = 0.088$ π mm.mrad, $\beta_x = 25.1$ m and $\alpha_x = -0.66$,
- $\epsilon_y = 0.086$ π mm.mrad, $\beta_y = 29.4$ m and $\alpha_y = -0.70$.

Thus, there is a good agreement between the two sets of measurements. When comparing these results to the ones obtained with 0703-300-28b, one notices that the normalized rms emittance $\epsilon^N = (\beta\gamma)\epsilon$ is conserved. At the entrance of QLB151, $\epsilon_x^N \approx 36.5\ \pi$ mm.mrad and $\epsilon_y^N \approx 38.0\ \pi$ mm.mrad. At the entrance of QNM273, one has $\epsilon_x^N \approx 42.6\ \pi$ mm.mrad and $\epsilon_y^N \approx 40.7\ \pi$ mm.mrad. The TRANSPORT simulations and the data taken in WBS28 when the current is varied in QNM273 have been compared in two situations : without and with the magnetic field in the solenoids. Figures 15 and 16 show again a rather fair agreement between calculations and measurements (on a better level when the solenoids are switched off though).

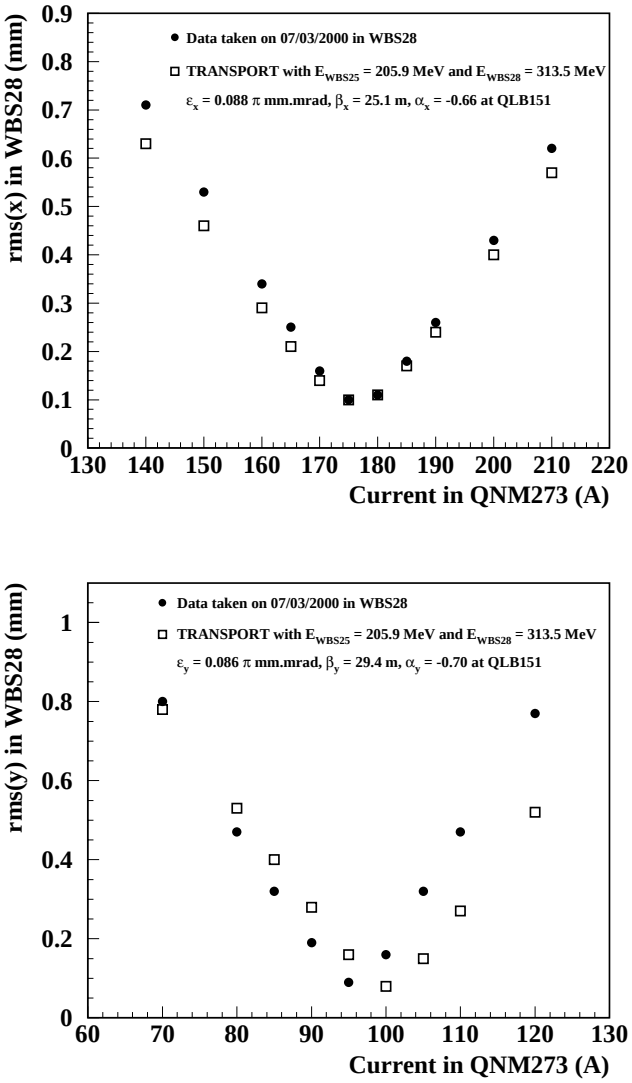

Figure 15: Variations of the rms of the horizontal and vertical beam profiles in WBS28 as a function of the current in QNM273 (TRANSPORT simulations and data). The magnetic field in SNL25 and SNL26 is switched off.

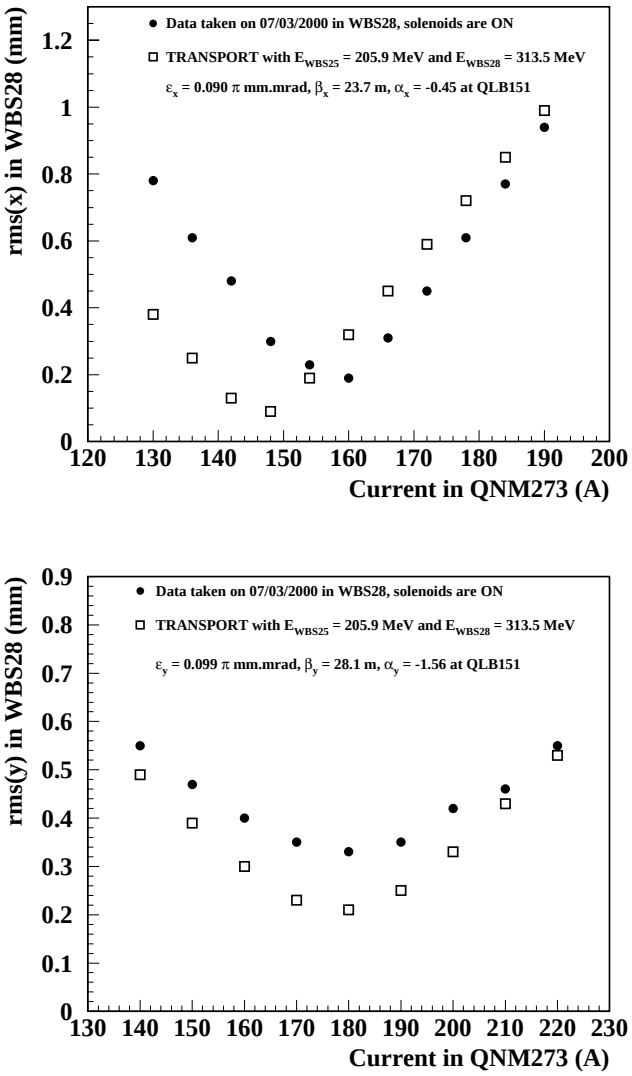

Figure 16: Variations of the rms of the horizontal and vertical beam profiles in WBS28 as a function of the current in QNM273 (TRANSPORT simulations and data). The magnetic field in SNL25 and SNL26 is switched on.

As for the dependence of our results on the energy after ACC25 and ACC26, it is negligible when the solenoids are switched off and rather weak when the solenoids are switched on, as illustrated by figure 17 (the Twiss parameters are no longer relevant when the solenoids are switched on, because of the coupling between the horizontal and vertical directions, so we only show the dependence of the rms on E).

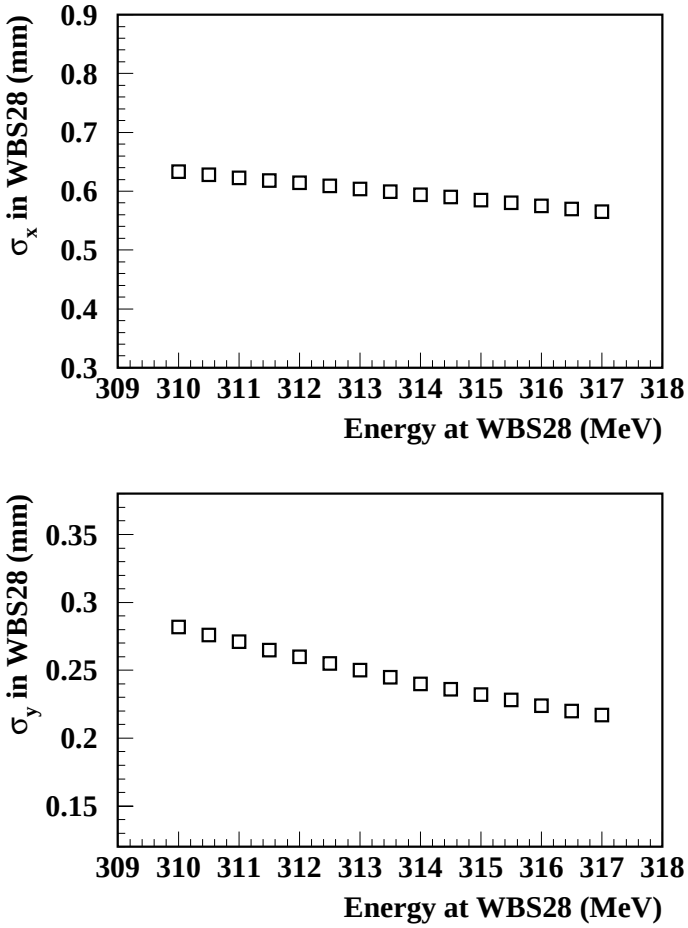

Figure 17: Variations of the rms of the beam in the horizontal and vertical directions with the energy at QNM273 (TRANSPORT simulation). At the entrance of QLB151, one has $\epsilon_x = 0.090$ π mm.mrad, $\beta_x = 23.7$ m, $\alpha_x = -0.45$, and $\epsilon_y = 0.099$ π mm.mrad, $\beta_y = 28.1$ m, $\alpha_y = -1.56$.

3.5 Conclusion and outlooks

In March 2000, we performed several measurements of the beam emittance and the Twiss parameters along LIL in order to test the reliability of the computer codes that we want to use for designing the CTF3 beam lines. A fair agreement was found between the predictions and the data, even if a high degree of accuracy could not be reached.

Besides this, a few problems were discovered and need to be solved before performing new measurements. For instance, switching on the magnetic field in the solenoids leads to a complex situation, since the horizontal and vertical directions are coupled, without reducing significantly the beam size for electrons. Since the lattice function measurements are not relevant anymore, one should preferably switch off the solenoids for the next MD

sessions. Also, the dependence of β and α on the beam energy should be significantly reduced by modifying the optics in order to avoid large variations of the Twiss parameters along the beam path, or the beam energy should be measured with a much better accuracy at the end of LIL-W.

4 Test of the wire beam scanners and calibration of the rf peak power meter

After the long shutdown and before this MD session, all WBS have been tested and each of them provided a good signal in the control room. However, the horizontal and vertical profiles were not checked with the beam itself. The experimental data coming from WBS28 gave inconsistent results when compared with simulations. After a careful check of all WBS, we found that WBS28 had its horizontal and vertical wires swapped. The correct situation has been implemented, so the experimental results are now consistent with the simulations, as described in section 3. Figure 18 shows beam profiles recorded in WBS28 with the correct settings.

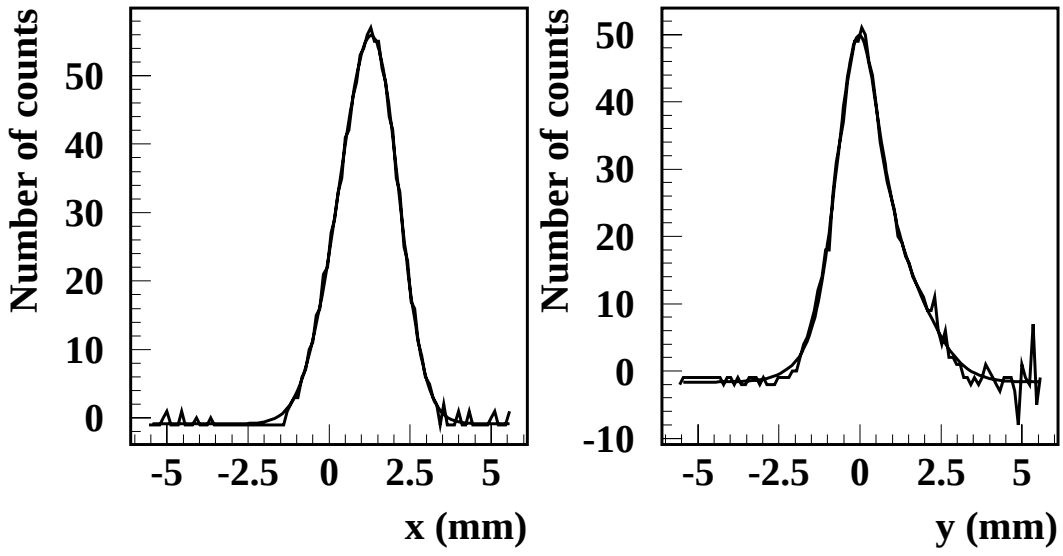

Figure 18: Horizontal and vertical beam profiles in WBS28 (8 March 2000).

The peak power meters (PPM) are used in order to measure the klystron output power. After the long shutdown, all PPM in LIL have been compared to a reference PPM and calibrated accordingly. Table 9 gives the measured output power and the corresponding energy gain for LIL. Only three modulators (MDK) are used to accelerate the electron beam.

Parameters	MDK13	MDK25	MDK31
PFN voltage (kV)	30.77	33.42	31.98
Klystron voltage (kV)	-219	-209	-230
Klystron current (A)	-230	-256	-229
Klystron power (MW)	20.9	24.5	26.3
Energy gain (MeV)	203	105	192

Table 9: LIl klystron parameters and energy gains.

The total energy gain is thus 500 MeV, which is the energy at which EPA works when the beam is injected and stored. However, the computed energy gain for MDK31 was not consistent with 192 MeV and thus needs to be checked.

5 Measurement of the EPA closed orbit

The closed orbit in EPA was measured in storage mode. The injection was set to one bunch every 80 ms. All dipole trims in EPA were at a current of 0 A. An intensity of $4.8 \cdot 10^{10}$ electrons was accumulated. The measurement was repeated for positrons with an intensity of $7.7 \cdot 10^{10}$ particles. Figure 19 shows the measured closed orbit.

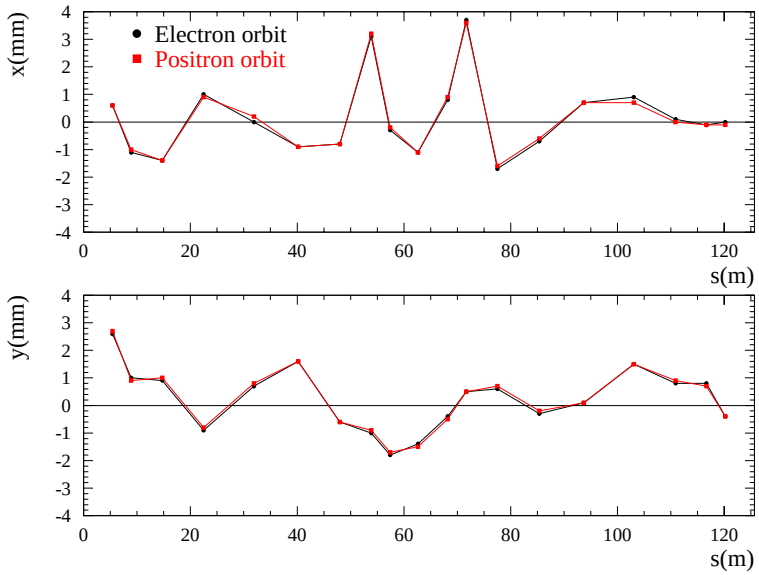

Figure 19: Measured horizontal and vertical closed orbits for electrons and positrons.

The horizontal orbit has a mean value of 0.15 mm with an RMS of 1.4 mm and a peak to peak difference of $\Delta x_{\mathrm{pk-pk}} = 5.4$ mm. The vertical orbit has a mean position of 0.24 mm with an RMS of 1.1 mm and a peak to peak difference of $\Delta y_{\mathrm{pk-pk}} = 4.4$ mm. The measured orbit was comparable to the orbit measured in 1999 ($\Delta x_{\mathrm{pk-pk}} = 5.2$ mm, $\Delta y_{\mathrm{pk-pk}} = 4.1$ mm) and is acceptable for the operation for LEP in the year 2000.

6 Conclusion and future measurements

During the March 2000 MD session, we took and analyzed data on the LIL machine. The bunch length has been measured at low charge. By including an uncorrelated energy spread of 1.86 MeV, we found a good agreement between measurements and calculations, with a bunch length of 7 ps FWHH. We also performed measurements of the lattice functions at three different points along LIL. We observed that the rms normalized emittance was conserved and that its value was about 40 π mm.mrad. As for the Twiss parameters, we compared our data to the predictions of the TRANSPORT simulation code and we found a good agreement. In addition to these measurements, we also performed some checks and corrections of the hardware systems.

The future measurements that we propose are the following ones :

- longitudinal beam dynamics in LIL : a measurement of the bunch length at the end of LIL-W (E = 500 MeV) is necessary to check the consistency of the data and the validity of our experimental method. One should also check the dependence of the bunch length on the charge. Finally, a comparison of the results obtained with our method and the results obtained using a streak camera is necessary. For future development, a two point measurement, in LIL and in EPA, is desirable : a comparison between these two points would help understand and manage the possible bunch lengthening in the transfer line between LIL and EPA.

- transverse beam dynamics in LIL : some TRANSPORT simulations indicated that the lattice functions can have a dependence on the beam energy and this should be checked experimentally. In the future, a new lattice will be designed and tested, in order to avoid or reduce the energy dependence of the Twiss parameters. It will also be interesting to check the correlation between the beam emittance and the charge of the bunches.

- beam dynamics in EPA : within the CTF3 framework, it is necessary to measure the bunch length in the EPA ring with a streak camera, in the nominal and isochronous cases, as well as for the minimum beam energy of EPA, which should be investigated around a value of 240 MeV. In EPA, the synchrotron frequency and the circumference are also of interest, so they should be measured experimentally.

- beam dynamics in the LIL to EPA transfer line : in the first step of CTF3, EPA will be an isochronous ring fed by LIL through the HIE transfer line. It is thus of first importance to check that our simulation codes can account for the lattice functions along the transfer line and, for this purpose, some measurements of the Twiss parameters are necessary near the injection point, using WBS82. Some tests of the transverse matching are also mandatory and, in order to perform them, three new quadrupoles need to have independent currents in the sections 35 and 36, in addition to QNM363.

References

[1] H. Braun et al., "The CLIC RF Power Source, a novel scheme of two-beam acceleration for electron-positron linear colliders", CERN Yellow Report 99-06, 1999.

[2] R. Corsini, J-P. Potier, L. Rinolfi, T. Risselada, J-C. Thomi, "First micro-bunch measurements in EPA as isochronous ring at 500 MeV", PS/LP Note 99-03 (MD).

[3] R. Corsini, L. Rinolfi, T. Risselada, J-C. Thomi, "report of the 1st June EPA MD", PS/LP Note 99-04 (MD).

[4] H. Braun, "Determination of LINAC V bunch length", private communication, 1989.

[5] Minutes of the CLIC RF Power Source meetings n° 63 (8 July 1999) and n° 66 (19 August 1999).

[6] LPI logbook n° 9, measurements performed on 5 April 1993.

[7] D.C. Carey, K.L. Brown, F. Rothacker, SLAC-R-95-462, Fermilab-Pub-95/069, UC-414, May 1995.